INTERNATIONAL JOURNAL FOR NUMERICAL METHODS IN FLUIDS
Int. J. Numer. Meth. Fluids 2008; **56**:485–506
Published online 6 June 2007 in Wiley InterScience (www.interscience.wiley.com). DOI: 10.1002/fld.1531

Simulation of transient gas flow at pipe-to-pipe intersections

Michael Herty*, † and Mohammed Seaïd

AG Technomathematik, Technische Universität Kaiserslautern, D-67663 Kaiserslautern, Germany

SUMMARY

We numerically investigate a well-established mathematical model for gas flow in pipeline networks. The emphasis is given to the description of coupling conditions at pipe-to-pipe intersections. The accurate prediction of these coupling conditions is essential in order to achieve good performance and reliable numerical simulations of network simulations. Nowadays, a variety of theoretical results for a reduced geometry exists. We conduct a numerical simulation of the two-dimensional representation at a pipe intersection. The results are used for verification and comparison with known theoretical results. High-order and non-oscillatory discretizations are used for solving the governing equations of gas flow. Verifications are conducted for two types of junctions to analyse the most adequate coupling conditions. Copyright © 2007 John Wiley & Sons, Ltd.

Received 30 November 2006; Revised 18 April 2007; Accepted 19 April 2007

KEY WORDS: gas flow; coupling conditions; non-oscillatory methods; pipeline networks

1. INTRODUCTION

During the last decade, there has been intense research in the field of transient gas flow of pipe networks in the mathematical as well as in the engineering community. Among the many references we refer to [1–14] and the publications of the pipeline interest group PSIG [15]. Currently, there exists a variety of approximate and simplified models most of them based on the isothermal Euler equations [7, 12] complemented by several numerical methods and approaches, see for example [11, 14, 16, 17]. Most of the previous work is focused on the correct modelling and simulation of the dynamics inside a pipe and only a few recent publications on pipe-to-pipe intersections

*Correspondence to: Michael Herty, AG Technomathematik, Technische Universität Kaiserslautern, D-67663 Kaiserslautern, Germany.
†E-mail: herty@mathematik.uni-kl.de

Contract/grant sponsor: German Research Foundation (DFG); contract/grant number: DFG Schwerpunktprogramm 1253

and pipe networks exist, see [9, 18, 19]. The most challenging part is the correct modelling of the dynamics near a pipe-to-pipe intersection since this influences most parts of the dynamics in the connected pipes. Typically, a pipe-to-pipe intersection, e.g. tee fitting, is assumed to be a single point (zero length). To obtain a well-posed problem, coupling conditions at the fitting have to be derived. These conditions will then yield boundary conditions for the isothermal Euler equations. Currently, there is a discussion on the correct coupling conditions for these models. For the sake of completeness, we collect some known and established coupling conditions. In the engineering community, usually conservation of mass and equal pressure directly at the point of intersection [7, 12, 20] is assumed. This has been investigated mathematically, e.g. in [9]. Sometimes refined models use tabulated values for so-called minor losses at pipe fittings [21]. Those tables depend on gas properties, geometry effects and have been fitted against by real-world data. From a mathematical point of view there is an alternative modelling of coupling conditions introduced in [18]. Therein, a mathematical study of coupling conditions which conserve mass and momentum has been conducted.

In this work we contribute to this discussion by a numerical study of an extended two-dimensional model. We investigate the detailed dynamics at the tee fitting. We assume that the dynamics inside each pipe are given by the transient isothermal Euler equations and resolve the detailed dynamics inside different types of pipe-to-pipe intersections with a robust numerical scheme as discussed below. The resolution is achieved by introducing a local zooming of the situation. This yields a two-dimensional domain representing the tee. Therein, we simulate the gas dynamics and finally average to obtain reference values. Those values are then compared to boundary values commonly used for isothermal Euler equations. We compare the simulation results with the analytical solutions which can be computed for constant gas states as in [9, 10, 18]. The comparison presented in the current work, shows the validity of the assumptions of equal pressure and conservation mass through a tee for the transient isothermal Euler equations under constraints on the initial data. Further, we found cases where neither the conservation of mass nor the conservation of momentum or pressure is guaranteed.

An important issue is the selection of the numerical scheme, which accurately resolves the two-dimensional equations in the considered tees. It is well known that the solutions of these equations present steep fronts, shocks and contact discontinuities, which need to be resolved accurately in applications and often cause severe numerical difficulties. High-order accurate schemes have become important in scientific computations because they offer a mean to obtain accurate solutions with less work that may be required for methods of lower accuracy. The literature is abundant for development of high-order methods for solving hyperbolic systems of conservation laws, among others we cite the weighted essentially non-oscillatory (WENO) methods [22, 23]. In the current work, we have implemented a fifth-order WENO scheme in the relaxation framework. First- and second-order relaxation schemes have been studied in [24, 25]. A variety of third-order relaxation schemes have also been developed in [26–28] for solving hyperbolic systems. The main advantage in considering combined relaxation WENO approach lies essentially on the semilinear structure of the relaxation system, which can be solved numerically without using Riemann solvers or characteristic decompositions.

The layout of the paper is as follows. In Section 2, we describe the governing equations used to model gas flow in pipeline networks. The coupling conditions at the pipeline junctions are discussed in Section 3. In Section 4, we formulate the numerical methods used for the solution procedure. Section 5 is devoted to numerical results for several test examples. We end the paper with few concluding remarks in Section 6.

DOI: 10.1002/fld

2. EQUATIONS FOR TRANSIENT GAS FLOW IN PIPELINE NETWORKS

In pipelines, the transient flow of gas is adequately described by a one-dimensional approach. The basic equations modelling the gas flow in pipes are derived from an equation of momentum, an equation of continuity, an equation of energy and state equation, see [1, 20, 29] among others. For practical applications, the form of the governing equations varies with respect to the assumptions made. Simplified models are usually obtained by neglecting certain dynamical aspects of the physical process, see [2] for an overview. In the current work, we focus on the full isothermal Euler equations which are considered as most detailed for gas flow in pipelines. To keep the presentation simple we assume that all pipes have the same diameter D and constant cross-sectional area. Furthermore, we assume constant temperature distribution Θ in the network, steady-state friction on all pipes and we neglect gravity effects by assuming horizontal pipes with zero slope. Hence, the continuity equation for natural gas flow is given by

$$\partial_t \rho_k + \partial_x(\rho_k u_k) = 0 \tag{1}$$

where ρ_k and u_k are the gas density and the gas velocity along the pipe k. The momentum equation for gas flow is

$$\partial_t(\rho_k u_k) + \partial_x(\rho_k u_k^2 + p_k) = -f_g \frac{\rho_k u_k |u_k|}{2D} \tag{2}$$

where p_k is the gas pressure in the pipe k and f_g is the friction factor for natural gas. The coefficient f_g can be calculated from the equation [30]

$$\frac{1}{\sqrt{f_g}} = -2\log\left(\frac{1}{3.7065}\frac{\varepsilon}{D} - 5.0452\frac{1}{Re}\log\left(\frac{1}{2.8257}\left(\frac{\varepsilon}{D}\right)^{1.1098} + \frac{5.8506}{0.8981}\frac{1}{Re}\right)\right) \tag{3}$$

where ε denotes the roughness coefficient of the pipe assumed to be equal for all pipes, and $Re = \bar{u}D/\nu$ denotes the Reynolds number defined by a reference velocity $\bar{u}$ and the gas kinematic viscosity ν. Other approaches for the friction term are also possible, e.g. the Darcy–Weisbach formula [20].

The gas flow model is closed by the equation of state

$$p_k = \frac{ZR\Theta}{M_g}\rho_k \tag{4}$$

where Z is the natural gas compressibility factor, R is the universal gas constant and M_g is the gas molecular weight. By defining the acoustic wave speed c as

$$c^2 = \frac{ZR\Theta}{M_g} \tag{5}$$

Equations (1) and (2) can be reformulated as

$$\begin{aligned} \partial_t \rho_k + \partial_x(\rho_k u_k) &= 0 \\ \partial_t(\rho_k u_k) + \partial_x(\rho_k u_k^2 + c^2\rho_k) &= -f_g \frac{\rho_k u_k |u_k|}{2D} \end{aligned} \tag{6}$$

DOI: 10.1002/fld

Equations (6) are known as isothermal Euler equations and describe transient fluid flow inside a pipe k where $k=1,\ldots,K$ where K is the total number of pipes in the network. We assume that each pipe k is represented by an interval $[a_k, b_k]$ for $k=1,\ldots,K$. If a pipe k is incoming or outgoing to the whole network we set $a_k=-\infty$ or $b_k=+\infty$, respectively.

To simulate a pipe network over a time interval $[0, T]$ Equations (6) have to be complemented by initial data (ρ_k^0, u_k^0) and appropriate boundary conditions at $x=a_k$ or b_k. As outlined in the introduction these conditions are obtained by prescribing coupling conditions at pipe fittings. We give the details in the next section.

3. COUPLING CONDITIONS AT THE PIPE-TO-PIPE FITTINGS

3.1. One-dimensional situation

Boundary conditions for system (6) are obtained by defining suitable coupling conditions at pipe-to-pipe intersections, see for example [7, 9]. In this section, we briefly describe these conditions and further discussions can be found in the abovementioned references. In a mathematical framework, the following conditions are commonly used in the literature [7, 9, 20].

Consider a single pipe-to-pipe fitting v where δ_v^- denotes indices of the incoming and δ_v^+ indices of the outgoing pipes as depicted in Figure 1. Hence,

(i) The mass is conserved through the intersection, i.e.

$$\sum_{k\in\delta_v^-}(\rho_k u_k)(b_k,t)=\sum_{k\in\delta_v^+}(\rho_k u_k)(a_k,t)\quad \forall t>0 \tag{7}$$

(ii) There is a single pressure at the intersection, i.e.

$$p(\rho_{\tilde{k}}(b_{\tilde{k}},t))=p(\rho_k(a_k,t)),\quad \forall(k,\tilde{k})\in\delta_v^-\times\delta_v^+\quad \forall t>0 \tag{8}$$

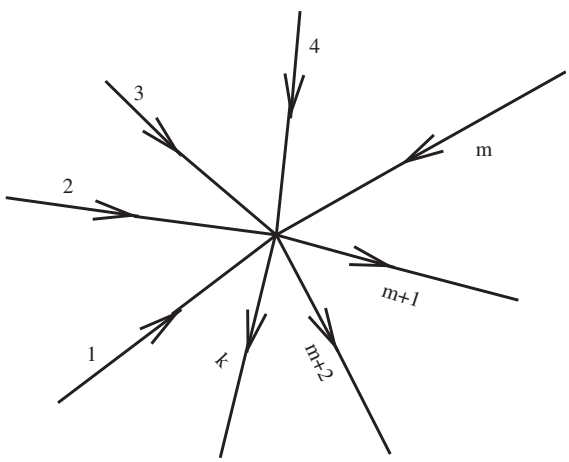

Figure 1. An illustration of pipe-to-pipe intersection in a network with m ingoing pipelines $\delta_v^-=\{1,2,\ldots,m\}$ and $K-m$ outgoing pipelines $\delta_v^+=\{m+1,m+2,\ldots,K\}$.

DOI: 10.1002/fld

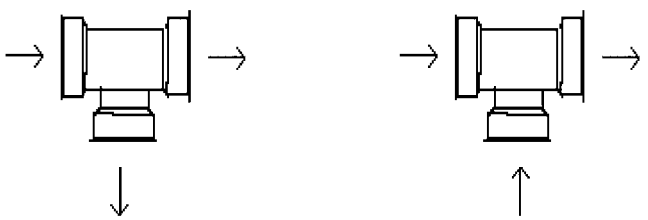

Figure 2. Schematic representation of two types of tee fittings and modelling in the network.

The two conditions (7) and (8) yield boundary conditions for all connected pipes at a_k and b_k, compare [9, 10]. Further, it has been proven that system (6) complemented with (7) and (8) is a mathematically well-posed problem provided the pipe-to-pipe fittings is a tee, i.e. a vertex v of degree three as schematically depicted in Figure 2 and provided that the initial data $\rho_k^0>0$ and $u_k^0\geqslant 0$ are piecewise constant. Alternatively, in [18] condition (ii) is replaced by

(ii′) There is a single momentum at the intersection, i.e.

$$p(\rho_{\tilde{k}}(b_{\tilde{k}},t))+(\rho_{\tilde{k}}u_{\tilde{k}}^2)(b_{\tilde{k}},t)=p(\rho_k(a_k,t))+(\rho_k u_k^2)(a_k,t)\quad \forall(k,\tilde{k})\in\delta_v^-\times\delta_v^+\ \ \forall t>0 \tag{9}$$

Again it has been proven [18] that system (6) complemented with (7) and (ii′) is a mathematically well-posed problem provided that the initial data $\rho_k^0>0$ and $u_k^0\geqslant 0$ are subsonic, i.e. $u_k^0\leqslant c$. Finally, we emphasize that in the engineering community the following condition is often used [1, 20].

The effect of the geometry on the coupling condition is accounted for by empirical factors $\tilde{f}$, which depend on the flow conditions as well as on the detailed geometry. Instead of requiring an equal pressure (8) a pressure loss is introduced.

(ii″) There exists a geometry and flow-dependent pressure loss $\tilde{f}_{\tilde{k},k}$, i.e.

$$p(\rho_{\tilde{k}}(b_{\tilde{k}},t))=p(\rho_k(a_k,t))-\tilde{f}_{\tilde{k},k}\quad \forall(k,\tilde{k})\in\delta_v^-\times\delta_v^+\ \ \forall t>0$$

Sometimes empirical data are used to estimate the value of the losses $\tilde{f}_{k,\tilde{k}}$.

3.2. Local two-dimensional situation

However, all previous conditions might not represent the physical behaviour at the intersections due to more complex gas interactions at pipe fitting. In the following, we propose a more detailed modelling and simulation to derive boundary conditions at pipe intersections. To keep the presentation simple and to compare later with analytical results we restrict the discussion to tee fittings. We introduce a zooming of the local situation at the intersection and consider a local two-dimensional situation. The zooming parameter to be introduced later is $D>0$. In the case of the tee in Figure 2 we obtain the schematic picture shown in Figure 3, where the pipe width is of order $2D$.

DOI: 10.1002/fld

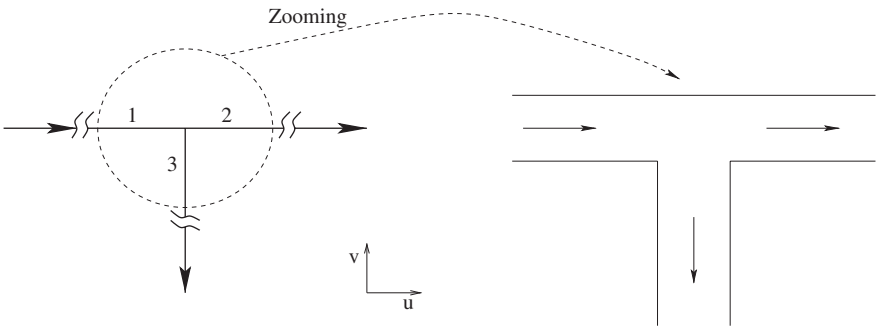

Figure 3. Zooming at a tee fittings and its corresponding two-dimensional domain.

The governing equations in this T-shaped spatial domain are the two-dimensional isothermal Euler equations

$$\begin{aligned}
&\partial_t \rho + \partial_x(\rho u) + \partial_y(\rho v) = 0\\
&\partial_t(\rho u) + \partial_x(\rho u^2 + c^2\rho) + \partial_y(\rho uv) = -f_g \frac{\rho u\sqrt{u^2+v^2}}{2D}\\
&\partial_t(\rho v) + \partial_x(\rho uv) + \partial_y(\rho v^2 + c^2\rho) = -f_g \frac{\rho v\sqrt{u^2+v^2}}{2D}
\end{aligned} \tag{10}$$

where u and v are the velocity components in x- and y-direction, respectively. This two-dimensional view is now used to obtain coupling conditions and then boundary conditions for (6). As in the theoretical studies reported in [9, 18] for Equations (6), we consider constant initial data ρ_k^0, u_k^0 for $k = 1$–3. These data are used to define initial values for Equations (10) as

$$\begin{pmatrix} \rho^0(x,y) \\ u^0(x,y) \\ v^0(x,y) \end{pmatrix} = \begin{cases} \begin{pmatrix} \rho_1^0 \\ u_1^0 \\ 0 \end{pmatrix} & \text{if } (x,y) \in]-\infty, 0[\times]0, 2D[\\ \begin{pmatrix} \rho_3^0 \\ u_3^0 \\ 0 \end{pmatrix} & \text{if } (x,y) \in]0, \infty[\times]0, 2D[\\ \begin{pmatrix} \rho_2^0 \\ 0 \\ u_2^0 \end{pmatrix} & \text{if } (x,y) \in]-D, D[\times]-\infty, 0[\end{cases} \tag{11}$$

where again $2D$ is the width of the connected pipes and the point $(x, y) = (0, 0)$ is at the intersection of all three pipes. We compute a well-developed solution $\rho = \rho(t, x, y)$, $u = u(t, x, y)$ and

DOI: 10.1002/fld

$v = v(t, x, y)$ of (10)–(11) for t sufficiently large. To obtain states which can be compared to a one-dimensional model we use volume averaging. We introduce the domains Ω_i^γ of size $2D \times \gamma$ and depending on a scaling parameter $\gamma > 0$. The domains correspond to the one-dimensional pipes

$$\begin{aligned}
\Omega_1^\gamma &= \{(x, y) : \ -\gamma \leqslant x \leqslant 0, \ 0 \leqslant y \leqslant 2D\} \\
\Omega_2^\gamma &= \{(x, y) : \ 0 \leqslant x \leqslant \gamma, \ 0 \leqslant y \leqslant 2D\} \\
\Omega_3^\gamma &= \{(x, y) : \ -D \leqslant x \leqslant D, \ -\gamma \leqslant y \leqslant 0\}
\end{aligned} \tag{12}$$

Then, we compute the volume averages of densities and velocities for $i = 1$–3 by

$$\begin{aligned}
\rho_i^\gamma &= \frac{1}{|\Omega_i^\gamma|} \int_{\Omega_i^\gamma} \rho(t, x, y) \, \mathrm{d}y \, \mathrm{d}x \\
u_i^\gamma &= \frac{1}{|\Omega_i^\gamma|} \int_{\Omega_i^\gamma} u(t, x, y) \, \mathrm{d}y \, \mathrm{d}x \\
v_i^\gamma &= \frac{1}{|\Omega_i^\gamma|} \int_{\Omega_i^\gamma} v(t, x, y) \, \mathrm{d}y \, \mathrm{d}x
\end{aligned} \tag{13}$$

Next, we let $\gamma \to \infty$ and obtain thereby functions $\gamma \to \rho_i^\gamma$ depending on the size of the domain Ω_i^γ. To resume the computations we use the combination of the following stopping criteria: in the theoretical discussion [9] the coupling conditions are such that, finally, waves emerge from the intersection. This can be mimiced in the two-dimensional representation by stopping the numerical simulation once emerging waves leave the domain of computation. Furthermore, we introduce a measure for the change in the averaged values: if $|\partial_\gamma \rho_i^\gamma| \leqslant \varepsilon$ for some γ_0 for some tolerance $\varepsilon > 0$, then we use this value $\rho_i^{\gamma_0}$ as numerical reference for the one-dimensional model, i.e. we set

$$\begin{aligned}
\rho_1(b_1) &:= \rho_1^{\gamma_0} \\
\rho_k(a_k) &:= \rho_k^{\gamma_0}, \quad k = 2, 3
\end{aligned} \tag{14}$$

for γ_0 such that $|\partial_\gamma \rho_i^{\gamma_0}| \leqslant \varepsilon$. Analogously, we proceed to obtain values $u_1(b_1)$ and $u_k(a_k)$ with $k = 2, 3$. Hence, we stop the computation either if $|\partial_\gamma \rho^\gamma|$ is small or once the waves left the computational domain. The obtained values ρ^γ are then compared with the theoretical predictions by investigating the relation between the values obtained in (14).

Remark 1
Some remarks are in order:

(i) The previous discussion focused on constant initial data since we later on compare with the analytical results, see Section 5. However, the approach is not limited to this case and general initial data can be considered.
(ii) The presentation has been given for a specific tee only, but is completely analogous in the other possible cases of a tee intersection, as the right plot in Figure 2, or more general geometries.
(iii) In Equation (10) we also have a friction term. However, in the network model (6) pipe fittings are considered as points of zero length. To obtain comparable numerical results we

DOI: 10.1002/fld

simulate (10) without friction effects $f_g = 0$, but we emphasize that the proposed approach is not limited to this case.

(iv) The local zooming could also be done for different geometries. However, most real-world fittings are of T-shape.

4. NUMERICAL METHODS AND SOLUTION PROCEDURE

Equations (6) can be solved using already existing software from computational fluid dynamics (CFD). Our focus in the present study is on investigating the coupling conditions described in the previous section rather than developing new numerical method for solving the partial differential equations (6). Therefore, we shall briefly highlight the schemes used for numerical solution of (6) and the main part of the present work is devoted to discuss the procedure used to verify the coupling conditions at pipeline junctions. For a single pipe, Equations (6) can be rewritten in a compact vector form as

$$\partial_t \mathbf{U} + \partial_x \mathbf{F}(\mathbf{U}) = \mathbf{Q}(\mathbf{U}) \tag{15}$$

where

$$\mathbf{U} = \begin{pmatrix} \rho \\ \rho u \end{pmatrix}, \quad \mathbf{F}(\mathbf{U}) = \begin{pmatrix} \rho u \\ \rho u^2 + c^2 \rho \end{pmatrix}, \quad \mathbf{Q}(\mathbf{U}) = \begin{pmatrix} 0 \\ -f_g \dfrac{\rho u |u|}{2D} \end{pmatrix}$$

Similarly, Equations (10) are rearranged as

$$\partial_t \mathbf{U} + \partial_x \mathbf{F}(\mathbf{U}) + \partial_y \mathbf{G}(\mathbf{U}) = \mathbf{Q}(\mathbf{U}) \tag{16}$$

where

$$\mathbf{U} = \begin{pmatrix} \rho \\ \rho u \\ \rho v \end{pmatrix}, \quad \mathbf{F}(\mathbf{U}) = \begin{pmatrix} \rho u \\ \rho u^2 + c^2 \rho \\ \rho u v \end{pmatrix}$$

$$\mathbf{G}(\mathbf{U}) = \begin{pmatrix} \rho v \\ \rho u v \\ \rho v^2 + c^2 \rho \end{pmatrix}, \quad \mathbf{Q}(\mathbf{U}) = \begin{pmatrix} 0 \\ -f_g \dfrac{\rho u \sqrt{u^2 + v^2}}{2D} \\ -f_g \dfrac{\rho v \sqrt{u^2 + v^2}}{2D} \end{pmatrix}$$

It is easy to verify that system (16) is hyperbolic with distinct eigenvalues given by

$$\begin{aligned} &\lambda^- = u - c, \quad \lambda^0 = u, \quad \lambda^+ = u + c \\ &\mu^- = v - c, \quad \mu^0 = v, \quad \mu^+ = u + c \end{aligned} \tag{17}$$

To discretize the equations in space we consider, for simplicity in presentation, a uniform control volume $[x_{i-1/2}, x_{i+1/2}] \times [y_{j-1/2}, y_{j+1/2}]$ with mesh sizes $\Delta x = x_{i+1/2} - x_{i-1/2}$ and

DOI: 10.1002/fld

$\Delta y = y_{j+1/2} - y_{j-1/2}$ in x- and y-direction, respectively. Integrating (16) over the control volume and keeping the time continuous we obtain the following semi-discrete system:

$$\frac{\mathrm{d}\mathbf{U}_{i,j}}{\mathrm{d}t} + \frac{\mathbf{F}(\mathbf{U}_{i+1/2,j}) - \mathbf{F}(\mathbf{U}_{i-1/2,j})}{\Delta x} + \frac{\mathbf{G}(\mathbf{U}_{i,j+1/2}) - \mathbf{G}(\mathbf{U}_{i,j-1/2})}{\Delta y} = \mathbf{Q}(\mathbf{U}_{i,j}) \tag{18}$$

where $\Psi_{i,j}$ is the space average of a generic function Ψ in the control volume $[x_{i-1/2}, x_{i+1/2}] \times [y_{j-1/2}, y_{j+1/2}]$

$$\Psi_{i,j} = \frac{1}{\Delta x}\frac{1}{\Delta y}\int_{x_{i-1/2}}^{x_{i+1/2}}\int_{y_{j-1/2}}^{y_{j+1/2}} \Psi(t, x, y)\,\mathrm{d}x\,\mathrm{d}y$$

whereas $\Psi_{i+1/2j} = \Psi(t, x_{i+1/2}, y_j)$ and $\Psi_{ij+1/2} = \Psi(t, x_i, y_{j+1/2})$ are the numerical fluxes at $(x_{i+1/2}, y_j)$ and $(x_i, y_{j+1/2})$, respectively. The spatial discretization is complete when a numerical reconstruction of the fluxes in (18) is chosen.

Let the time interval $[0, T]$ be divided into subintervals $[t_n, t_{n+1}]$ of length Δt such that $t_n = n\Delta t$ and we denote $\Psi^n_{i,j} = \Psi_{i,j}(t_n)$. The procedure to advance the solution of (18) from the time t_n to the next time t_{n+1} can be carried out as

$$\begin{aligned}
\mathbf{U}^{(1)}_{i,j} &= \mathbf{U}^n_{i,j} + \Delta t\mathbf{R}(\mathbf{U}^n_{i,j}) \\
\mathbf{U}^{(2)}_{i,j} &= \tfrac{3}{4}\mathbf{U}^n_{i,j} + \tfrac{1}{4}\mathbf{U}^{(1)}_{i,j} + \tfrac{1}{4}\Delta t\mathbf{R}(\mathbf{U}^{(1)}_{i,j}) \\
\mathbf{U}^{n+1}_{i,j} &= \tfrac{1}{3}\mathbf{U}^n_{i,j} + \tfrac{2}{3}\mathbf{U}^{(2)}_{i,j} + \tfrac{2}{3}\Delta t\mathbf{R}(\mathbf{U}^{(2)}_{i,j})
\end{aligned} \tag{19}$$

where $\mathbf{R}$ stands for the right-hand side in (18), i.e.

$$\mathbf{R}(\mathbf{U}_{i,j}) = -\frac{\mathbf{F}(\mathbf{U}_{i+1/2,j}) - \mathbf{F}(\mathbf{U}_{i-1/2,j})}{\Delta x} - \frac{\mathbf{G}(\mathbf{U}_{i,j+1/2}) - \mathbf{G}(\mathbf{U}_{i,j-1/2})}{\Delta y} + \mathbf{Q}(\mathbf{U}_{i,j})$$

This class of explicit time integration schemes has become popular in CFD algorithms, see for example [31, 32]. The nice feature of this method lies on the fact that (19) is a convex combination of first-order Euler steps which exhibit strong stability properties. Therefore, the scheme (19) is TVD, third-order accurate in time, and stable under the usual hyperbolic CFL conditions.

4.1. Spatial discretization

In order to reconstruct the numerical fluxes in the semi-discrete system (18), we consider a relaxation-based method. This method reconstructs the fluxes without relying on Riemann problem solvers and can be used with arbitrary order of accuracy. The first- and second-order relaxation methods were first proposed in [24] to solve hyperbolic systems of conservation laws. A third-order relaxation scheme has also been proposed in [25] and intensively tested in [26–28] for a wide hyperbolic systems of conservation laws. The third-order method in the above-mentioned references reconstructs the fluxes in (18) using linear combination of small stencils such that the overall combination preserves the third-order accuracy. In the present work, we formulate a fifth-order reconstruction for the numerical fluxes in (18). The key idea is to replace the linear weights in the third-order reconstruction by nonlinear weights capable of reducing the spurious oscillations that usually develop in regions with discontinuous derivatives.

DOI: 10.1002/fld

Associated with Equations (16) a relaxation approximation is

$$\begin{aligned}\partial_t \mathbf{U} + \partial_x \mathbf{V} + \partial_y \mathbf{W} &= \mathbf{Q}(\mathbf{U})\\ \partial_t \mathbf{V} + \mathbf{A}^2 \partial_x \mathbf{U} &= -\frac{1}{\varepsilon}(\mathbf{V} - \mathbf{F}(\mathbf{U}))\\ \partial_t \mathbf{W} + \mathbf{B}^2 \partial_y \mathbf{U} &= -\frac{1}{\varepsilon}(\mathbf{W} - \mathbf{G}(\mathbf{U}))\end{aligned} \tag{20}$$

where $\mathbf{V} \in \mathbb{R}^3$ and $\mathbf{W} \in \mathbb{R}^3$ are relaxation variables, $\mathbf{A}^2$ and $\mathbf{B}^2$ are diagonal matrices in $\mathbb{R}^3 \times \mathbb{R}^3$ where their entries A_l^2 and B_l^2 are characteristic speeds of (16). The relaxation system (20) has a typical semilinear structure with linear characteristic variables defined by

$$\mathscr{F}^{\pm} = \mathbf{V} \pm \mathbf{A}\mathbf{U} \quad \text{and} \quad \mathscr{G}^{\pm} = \mathbf{W} \pm \mathbf{B}\mathbf{U} \tag{21}$$

Formally, in the zero relaxation limit $\varepsilon \longrightarrow 0$, we recover the original system (16) provided the subcharacteristic condition [24]

$$\frac{|\mathbf{F}_l'(\mathbf{U})|}{\mathbf{A}_l} + \frac{|\mathbf{G}_l'(\mathbf{U})|}{\mathbf{B}_l} \leqslant 1 \quad \forall l = 1, 2, 3 \tag{22}$$

holds in (20). It is easy to verify that if we project the relaxation variables into the local equilibrium

$$\mathbf{V} = \mathbf{F}(\mathbf{U}) \quad \text{and} \quad \mathbf{W} = \mathbf{G}(\mathbf{U}) \tag{23}$$

then the first equation in (20) reduces to the original conservation laws (16). From a numerical view point, it is simpler to solve system (20) than the original equations (16). Here, our fifth-order reconstruction is applicable directly to the linear characteristic variables (21). In what follows we only formulate $\mathbf{U}_{i+1/2,j}$ and $\mathbf{V}_{i+1/2,j}$, and expressions for other fluxes are obtained in an entirely analogous manner.

Since the variables $\mathscr{F}^+$ and $\mathscr{F}^-$ travel along constant characteristics with speeds $+A$ and $-A$, respectively, a WENO reconstruction can be easily applied to them. Thus, the numerical fluxes $\mathscr{F}^{\pm}_{i+1/2,j}$ at the cell boundary $(x_{i+1/2}, y_j)$ are defined as left and right extrapolated values $\mathscr{F}^{+,\mathrm{L}}_{i+1/2,j}$ and $\mathscr{F}^{-,\mathrm{R}}_{i+1/2,j}$ by

$$\mathscr{F}^{+}_{i+1/2,j} = \mathscr{F}^{+,\mathrm{L}}_{i+1/2,j}, \quad \mathscr{F}^{-}_{i+1/2,j} = \mathscr{F}^{-,\mathrm{R}}_{i+1/2,j} \tag{24}$$

These extrapolated values are obtained from cell averages by means of high-order WENO polynomial reconstruction. Here, we use the fifth-order WENO reconstruction proposed in [23]. Higher-order reconstructions are also possible, such as those developed in [22]. For the generic function $\Psi(x, y)$, the fifth-order accurate left boundary extrapolated value $\Psi^{\mathrm{L}}_{i+1/2,j}$ is defined as

$$\Psi^{\mathrm{L}}_{i+1/2,j} = \omega_0 \mathscr{V}_0 + \omega_1 \mathscr{V}_1 + \omega_2 \mathscr{V}_2 \tag{25}$$

where $\mathscr{V}_r$ is the extrapolated value obtained from cell averages in the rth stencil $(i-r, i-r+1, i-r+2)$ in x-direction

$$\begin{aligned}\mathscr{V}_0 &= \tfrac{1}{6}(-\Psi_{i+2,j} + 5\Psi_{i+1,j} + 2\Psi_{i,j})\\ \mathscr{V}_1 &= \tfrac{1}{6}(-\Psi_{i-1,j} + 5\Psi_{i,j} + 2\Psi_{i+1,j})\\ \mathscr{V}_2 &= \tfrac{1}{6}(2\Psi_{i-2,j} - 7\Psi_{i-1,j} + 11\Psi_{i,j})\end{aligned}$$

DOI: 10.1002/fld

and ω_r, $r=0, 1, 2$, are nonlinear WENO weights given by

$$\omega_k = \frac{\alpha_k}{\sum_{l=0}^{2} \alpha_l}, \quad \alpha_0 = \frac{3}{10(\tau + \mathrm{IS}_0)^2}, \quad \alpha_1 = \frac{3}{5(\tau + \mathrm{IS}_1)^2}, \quad \alpha_2 = \frac{1}{10(\tau + \mathrm{IS}_2)^2} \tag{26}$$

Here the parameter τ is introduced to guarantee that the denominator does not vanish and is empirically taken to be 10^{-6}. The smoothness indicators IS_r, $r=0, 1, 2$, are given by [23]

$$\mathrm{IS}_0 = \tfrac{13}{12}(\Psi_{i,j} - 2\Psi_{i+1,j} + \Psi_{i+2,j})^2 + \tfrac{1}{4}(3\Psi_{i,j} - 4\Psi_{i+1,j} + \Psi_{i+2,j})^2$$
$$\mathrm{IS}_1 = \tfrac{13}{12}(\Psi_{i-1,j} - 2\Psi_{i,j} + \Psi_{i+1,j})^2 + \tfrac{1}{4}(\Psi_{i-1,j} - \Psi_{i+1,j})^2$$
$$\mathrm{IS}_2 = \tfrac{13}{12}(\Psi_{i-2,j} - 2\Psi_{i-1,j} + \Psi_{i,j})^2 + \tfrac{1}{4}(\Psi_{i-2,j} - 4\Psi_{i-1,j} + 3\Psi_{i,j})^2$$

The right value $\Psi^{\mathrm{R}}_{i+1/2,j}$ is obtained by symmetry as

$$\Psi^{\mathrm{R}}_{i+1/2,j} = \omega_0 \mathscr{V}_0 + \omega_1 \mathscr{V}_1 + \omega_2 \mathscr{V}_2 \tag{27}$$

where

$$\mathscr{V}_0 = \tfrac{1}{6}(2\Psi_{i+3,j} - 7\Psi_{i+2,j} + 11\Psi_{i+1,j})$$
$$\mathscr{V}_1 = \tfrac{1}{6}(-\Psi_{i+2,j} + 5\Psi_{i+1,j} + 2\Psi_{i,j})$$
$$\mathscr{V}_2 = \tfrac{1}{6}(-\Psi_{i-1,j} + 5\Psi_{i,j} + 2\Psi_{i+1,j})$$

The corresponding weights and smoothness indicators are given by (26) with

$$\mathrm{IS}_0 = \tfrac{13}{12}(\Psi_{i+1,j} - 2\Psi_{i+2,j} + \Psi_{i+3,j})^2 + \tfrac{1}{4}(3\Psi_{i+1,j} - 4\Psi_{i+2,j} + \Psi_{i+3,j})^2$$
$$\mathrm{IS}_1 = \tfrac{13}{12}(\Psi_{i,j} - 2\Psi_{i+1,j} + \Psi_{i+2,j})^2 + \tfrac{1}{4}(\Psi_{i,j} - \Psi_{i+2,j})^2$$
$$\mathrm{IS}_2 = \tfrac{13}{12}(\Psi_{i-1,j} - 2\Psi_{i,j} + \Psi_{i+1,j})^2 + \tfrac{1}{4}(\Psi_{i-1,j} - 4\Psi_{i,j} + 3\Psi_{i+1,j})^2$$

Once $\mathscr{F}^+_{i+1/2,j}$ and $\mathscr{F}^-_{i+1/2,j}$ are reconstructed in (24), the numerical fluxes $\mathbf{U}_{i+1/2,j}$ and $\mathbf{V}_{i+1/2,j}$ in the relaxation system are obtained from (21) by

$$\mathbf{U}_{i+1/2,j} = \frac{1}{2A_{i+1/2,j}}(\mathscr{F}^+_{i+1/2,j} - \mathscr{F}^-_{i+1/2,j}), \quad \mathbf{V}_{i+1/2,j} = \frac{1}{2}(\mathscr{F}^+_{i+1/2,j} + \mathscr{F}^-_{i+1/2,j}) \tag{28}$$

Analogously, the numerical fluxes $\mathbf{U}_{i,j+1/2}$ and $\mathbf{W}_{i,j+1/2}$ are obtained from $\mathscr{G}^+_{i,j+1/2}$ and $\mathscr{G}^-_{i,j+1/2}$ as

$$\mathbf{U}_{i,j+1/2} = \frac{1}{2B_{i,j+1/2}}(\mathscr{G}^+_{i,j+1/2} + \mathscr{G}^-_{i,j+1/2}), \quad \mathbf{W}_{i,j+1/2} = \frac{1}{2}(\mathscr{G}^+_{i,j+1/2} + \mathscr{G}^-_{i,j+1/2}) \tag{29}$$

Note that the above local auxiliary variables, introduced to approximate the derivatives of the solution, are superficial and can be easily removed for linear problems. Clearly, the accuracy of the relaxation method will depend on the choice of the characteristic speeds $A_{i+1/2,j}$ and $B_{i,j+1/2}$ in (28) and (29), respectively.

DOI: 10.1002/fld

4.2. Solution procedure

For wide enough pipes, the friction terms in (10) become negligible. Thus, the numerical method described in the previous section is used to solve the frictionless two-dimensional Euler equations (10) in the computational domain shown in Figure 4. Here, using the pipe diameter D as a reference length, the domain is $4D$ high and $7D$ wide. Initial conditions are taken as

$$\begin{pmatrix} \rho(0,x,y) \\ u(0,x,y) \\ v(0,x,y) \end{pmatrix} = \begin{cases} \begin{pmatrix} \rho_1 \\ u_1 \\ 0 \end{pmatrix} & \text{in Pipe 1} \\ \begin{pmatrix} \rho_2 \\ u_2 \\ 0 \end{pmatrix} & \text{in Pipe 2} \\ \begin{pmatrix} \rho_3 \\ 0 \\ v_3 \end{pmatrix} & \text{in Pipe 3} \end{cases} \tag{30}$$

Other pipe intersections can be handled in a similar manner. No-slip boundary conditions are imposed on the solid walls and homogeneous Neumann conditions are used for the open boundaries. The corner of the right step is a singular point and we treat it in the same way as in [33]. The characteristic speeds $A_{i+1/2,j}$ and $B_{i,j+1/2}$ in (28) and (29) can be chosen based on rough estimates of eigenvalues (17). Other choice is to calculate the characteristic speeds locally at each control volume $[x_{i-1/2}, x_{i+1/2}] \times [y_{j-1/2}, y_{j+1/2}]$ as

$$A_{i+1/2,j} = \max\{|\lambda^{\mathrm{L}}_{i+1/2,j}|, |\lambda^{\mathrm{R}}_{i+1/2,j}|\}, \quad B_{i,j+1/2} = \max\{|\mu^{L}_{i,j+1/2}|, |\mu^{\mathrm{R}}_{i,j+1/2}|\} \tag{31}$$

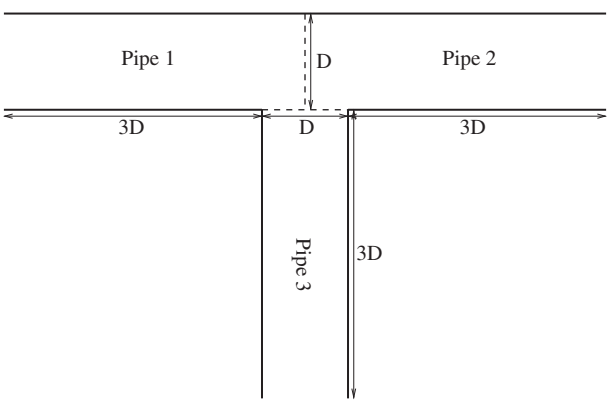

Figure 4. Spatial domain used for the two-dimensional computations.

DOI: 10.1002/fld

A global selection is simply to take the maximum over the gridpoints in (31) as

$$A = \max_{i,j}(A_{i+1/2,j}), \quad B = \max_{i,j}(B_{i,j+1/2}) \tag{32}$$

It should be stressed that larger values of $A_{i+1/2,j}$ and $B_{i,j+1/2}$ usually add more numerical dissipation to the relaxation scheme.

4.3. Theoretical results

The comparison between the results obtained by the numerical simulation and the analytical results is presented in Section 5.2 and here we only comment on necessary assertions of the underlying theory. Currently, only for the coupling conditions (7) and (8), analytical results for different initial data exist, compare [9], but there are no explicit expressions for conditions (7) and (9). The analytical solution for a one-dimensional pipe model in [9] relies on the hypothesis that the pressure is constant at the tee intersection, that the mass is conserved and the flow direction does not change. The aim of the presented simulations is to verify these assumptions which are commonly imposed in many engineering applications. We simulate different inflow configurations for two types of tee intersections with three connected pipes. We stop the two-dimensional simulation whenever a wave exits the computational domain. This corresponds to the analytical discussion where only waves of negative (respectively positive) speed emerge from the pipe-to-pipe intersection. In the second stage, we average the computed results to obtain equivalent one-dimensional fluxes and pressures for each pipe (referred to as simulation results in the sequel) and compare these values with the analytical results obtained in [9]. Due to additional geometry effects in the two-dimensional simulation we do not expect a full coincidence in the analytical and simulation results. But we are looking for a verification of the underlying principle of conservation of mass and equal pressure at the tee intersections. Furthermore, we expect both the analytical and simulation results to behave in a similar way when changing the initial conditions.

5. NUMERICAL EXAMPLES AND RESULTS

In this section, we examine the accuracy of the proposed schemes for several different situations and verify the coupling conditions at junctions in pipeline networks. Our test examples can be considered in two general categories. We first perform an accuracy test for the fifth-order scheme. Secondly, we test the ability of our scheme to verify the coupling conditions for two types of junctions in a pipeline network. All the results presented in this section are obtained using the relaxed method ($\varepsilon = 0$) using the local characteristic speeds (31). In all our computations the CFL number is fixed to 0.75 and time steps Δt are calculated according to the stability condition

$$\Delta t = \mathrm{CFL} \min\left(\frac{\Delta x}{|A^2_{i+1/2,j}|}, \frac{\Delta y}{|B^2_{i,j+1/2}|}\right) \tag{33}$$

5.1. Accuracy test examples

First, we check the accuracy of the relaxation scheme for the scalar advection equation

$$\partial_t u + \partial_x u = 0, \quad x \in [-1, 1] \tag{34}$$

DOI: 10.1002/fld

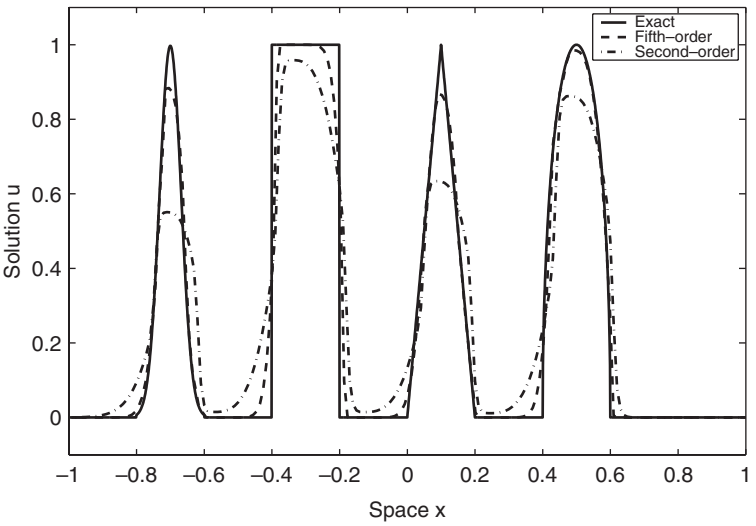

Figure 5. Results for the one-dimensional linear advection equation at $t = 6$.

subject to periodic boundary condition and the following initial condition:

$$u(x,0) = \begin{cases} \dfrac{1}{\sqrt{0.32\pi}} \mathrm{e}^{-500(x+0.7)^2} & \text{if } -0.8 \leqslant x \leqslant -0.6 \\ 1 & \text{if } -0.4 \leqslant x \leqslant -0.2 \\ 1 - |10x - 1| & \text{if } 0.0 \leqslant x \leqslant 0.2 \\ \sqrt{1 - 100(x - 0.5)^2} & \text{if } 0.4 \leqslant x \leqslant 0.6 \\ 0 & \text{otherwise} \end{cases} \tag{35}$$

This test example is used to assess different features of the fifth-order relaxation scheme such as accuracy in smooth regions and discontinuous resolution. Note that the solution of the linear problem (34)–(35) includes a smooth but narrow combination of Gaussian, square, sharp triangle and half-ellipse waves. The time necessary for a complete wave period is $t = 2$. In Figure 5 we present the numerical solution obtained at time $t = 6$ using uniform grid with 200 gridpoints. For comparison reasons we also include the result obtained using the second-order relaxation method developed in [24].

From the results presented in Figure 5 we observe that the second-order scheme resolves this advection problem poorly. For instance, excessive numerical dissipation has been introduced by the second-order scheme for the Gaussian, triangle and half-ellipse waves. We see that the fifth-order scheme is clearly superior to the second-order scheme. In particular, on the peak resolution in triangular profile the fifth-order scheme produces the most accurate results.

DOI: 10.1002/fld

Table I. Error-norms for the one-dimensional isothermal Euler system.

Gridpoints	L^∞-error	Rate	L^1-error	Rate
40	0.17207E−00	—	0.10263E−00	—
80	0.13678E−01	3.653	0.65947E−02	3.960
160	0.86325E−02	3.986	0.34324E−03	4.264
320	0.30795E−04	4.809	0.10741E−04	4.998
640	0.94450E−06	5.027	0.30188E−06	5.153

Our next concern is to check the accuracy of our scheme for a nonlinear system of conservation laws. To this end, we solve the one-dimensional isothermal Euler system of inviscid gas dynamics

$$\begin{aligned} \partial_t \rho + \partial_x(\rho u) &= 0 \\ \partial_t(\rho u) + \partial_x(\rho u^2 + p) &= 0 \end{aligned} \tag{36}$$

We solve the inviscid Euler system (36) in space domain $[-\pi, \pi]$ with periodic boundary conditions. Initial data are obtained from the smooth exact solution

$$\rho(x,t) = 1 + 0.2\sin(x-t), \quad u(x,t) = 1, \quad p(x,t) = 1 \tag{37}$$

Table I shows a convergence study in the L^∞- and L^1-error norms for the fifth-order scheme. The errors are calculated at time $t = 1$ by the difference between the point values of the exact solution and the reconstructed point values of the computed density solution. As expected, the proposed relaxation scheme preserves the fifth-order accuracy for this nonlinear system.

5.2. Verification of coupling conditions

This section is devoted to numerically verify the coupling conditions described in the present work. We consider the two types of tee fittings illustrated in Figure 2, namely, one pipe with ingoing flow and two pipes with outgoing flow (referred to as 1-to-2 situation) for the first example. For the second example, two pipes with ingoing flow and one pipe with outgoing flow (referred to as 2-to-1 situation) are considered. The pipe diameter is fixed to $D = 0.5$ in all our computations and different initial conditions (30) are tested. For each simulation time, the pressure, density and velocity solutions are stored and examined. We emphasize that we do not expect the same final values from the simulation and the theoretical investigations due to the more complex two-dimensional dynamics. We qualitatively compare the averaged values obtained by simulation (14) and the theoretical predictions.

To verify the resolution of our numerical scheme we first check the grid dependence of the solutions. To this end, we solve the 1-to-2 situation subject to the following initial conditions:

$$\rho_1 = 2, \quad \rho_2 = 3, \quad \rho_3 = 4; \quad u_1 = 5, \quad u_2 = 1.666; \quad v_3 = -1.5 \tag{38}$$

Figure 6 shows the grid effects on profiles of density and u-velocity at the mid-width of each pipe using five different meshes with uniform spatial stepsizes $\Delta x = \Delta y = h$, where $h = 0.08, 0.04, 0.02, 0.01$ and 0.005. The results in Figure 6 are displayed at time $t = 0.1$. It is easy to see that solutions obtained using the mesh with $h = 0.08$ are far from those obtained by the other meshes. Decreasing the spatial step size, results for the mesh with $h = 0.01$ and the mesh with $h = 0.005$ are roughly

DOI: 10.1002/fld

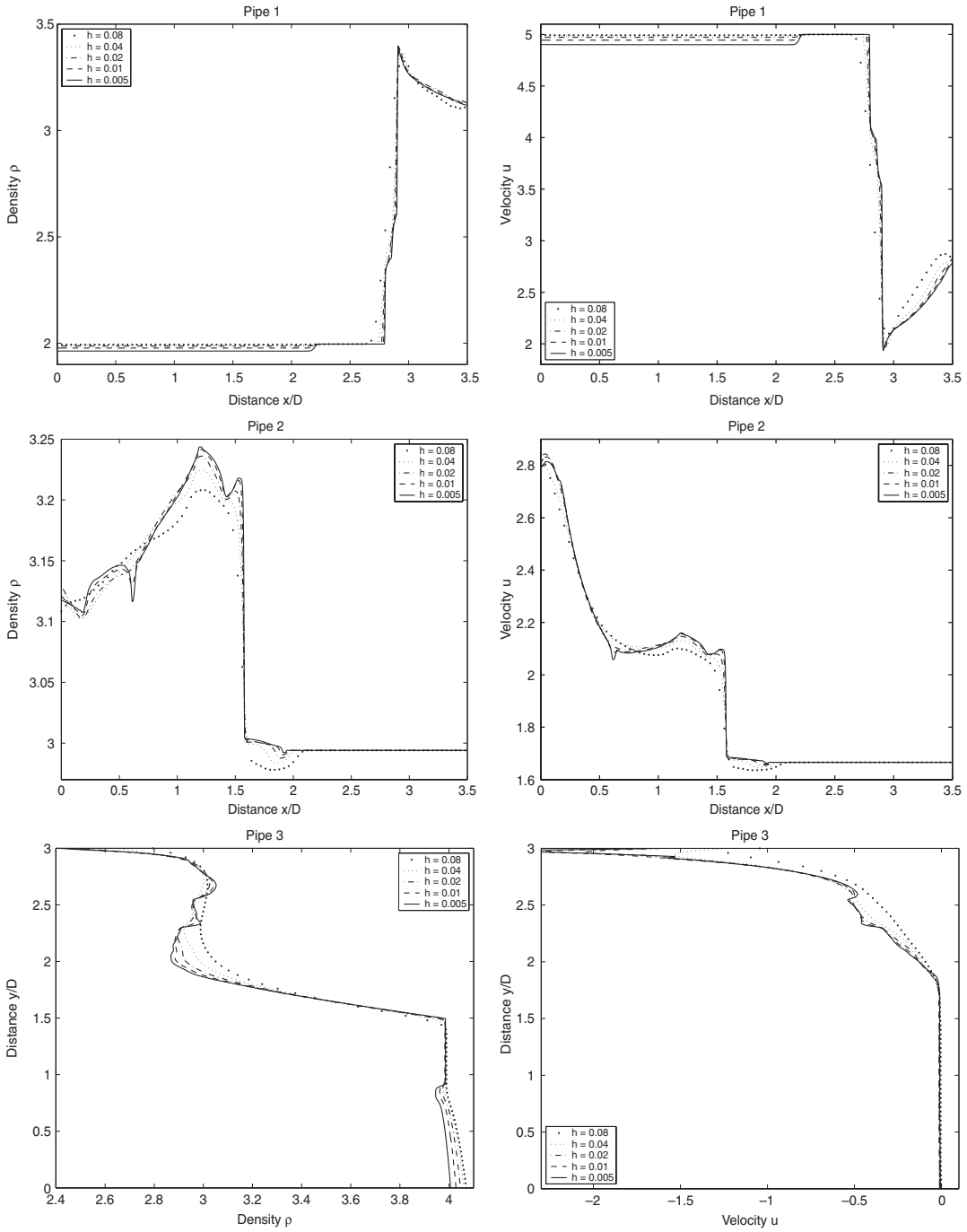

Figure 6. Cross sections of density (left) and u-velocity for the 1-to-2 situation at time $t = 0.1$.

DOI: 10.1002/fld

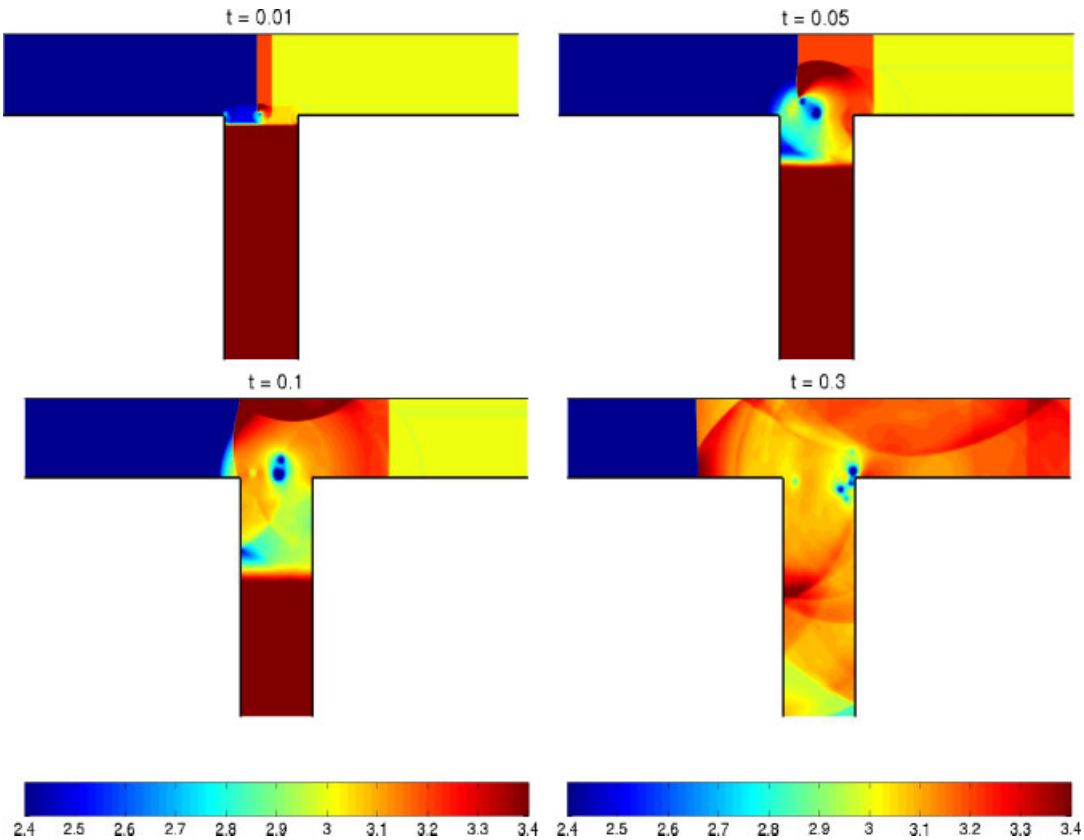

Figure 7. Density snapshots for the 1-to-2 situation at four different times.

similar. Similar behaviour has been observed for the 2-to-1 situation. These results ensure grid independence of the numerical results. Therefore, bearing in mind the slight change in the results from the mesh with $h = 0.01$ and the mesh with $h = 0.005$ at the expense of rather significant increase in the computational cost, the mesh with $h = 0.01$ is believed to be adequate to obtain the results free of grid effects. Hence, our next simulations are performed using the mesh with $h = 0.01$. A similar result is obtained for the 2-to-1 situation and we do not give the details here.

Further, we show the evolution of the two-dimensional dynamics on one sample initial data showing the capturing of small circulations by our numerical scheme. Figure 7 displays snapshots of the density at four different times $t = 0.01, 0.05, 0.1$ and 0.3 using the initial conditions (38). As can be seen, low-density regions are generated in the tee intersection and are recirculated during the simulation time. At the final time, these recirculation zones are accumulated near the corner of the right step. Our high-order relaxation scheme captures accurately the evolution of the interface in the computational domain without diffusing the fronts or introducing oscillations near steep gradients.

After verifying the numerical solution procedure we turn to the comparison of the averaged values as explained in Section 3.2 for different initial conditions. First, we consider the 1-to-2

DOI: 10.1002/fld

Table II. Verification of coupling conditions for the 1-to-2 situation.

	$\rho_1 = 2$	$\rho_1 = 2.4$	$\rho_1 = 2.8$	$\rho_1 = 3$	$\rho_1 = 3.4$	$\rho_1 = 3.8$	$\rho_1 = 4$
Pressure in the three pipes							
Pipe 1	109.7044	118.0256	125.2863	127.3167	135.2049	141.9893	142.8606
	(114.817)	(122.111)	(128.592)	(131.591)	(137.198)	(142.368)	(144.815)
Pipe 2	113.2206	120.4299	127.6552	129.2772	135.8529	140.8409	143.4291
	(114.817)	(122.111)	(128.592)	(131.591)	(137.198)	(142.368)	(144.815)
Pipe 3	115.7017	121.4958	127.2871	130.1011	136.5938	141.9951	143.6773
	(114.817)	(122.111)	(128.592)	(131.591)	(137.198)	(142.368)	(144.815)
Flux in the three pipes							
Pipe 1	9.08376	11.14579	13.19811	14.20330	16.15881	18.04243	18.97299
	(6.9352)	(9.88412)	(12.6283)	(13.9365)	(16.4441)	(18.8266)	(19.977)
Pipe 2	6.55352	7.61451	8.68304	9.22067	10.28872	11.32219	11.82324
	(6.48497)	(8.15181)	(9.69579)	(10.4298)	(11.834)	(13.1651)	(13.8068)
Pipe 3	2.53080	3.53345	4.51625	4.98597	5.87229	6.72410	7.15516
	(0.45022)	(1.73231)	(2.9325)	(3.50661)	(4.61009)	(5.66158)	(6.17018)

Note: We vary the density ρ_1 and we keep other variables fixed. The values in parenthesis refer to the analytical results.

Table III. Verification of coupling conditions for the 1-to-2 situation.

	$u_1 = 4$	$u_1 = 5$	$u_1 = 6$	$u_1 = 6.5$	$u_1 = 7.5$	$u_1 = 8.5$	$u_1 = 9$
Pressure in the three pipes							
Pipe 1	115.2418	118.3104	120.8469	122.1585	124.8776	127.3623	128.5093
	(124.492)	(131.586)	(139.071)	(142.965)	(151.065)	(159.597)	(164.028)
Pipe 2	115.0216	118.2603	120.8546	122.0521	124.4525	126.8142	127.9266
	(124.492)	(131.586)	(139.071)	(142.965)	(151.065)	(159.597)	(164.028)
Pipe 3	117.0552	119.1032	121.9611	123.4902	125.6128	128.5010	129.8158
	(124.492)	(131.586)	(139.071)	(142.965)	(151.065)	(159.597)	(164.028)
Flux in the three pipes							
Pipe 1	11.24882	14.20343	17.25383	18.81524	21.96851	25.06985	26.62007
	(10.8814)	(13.9368)	(17.3021)	(19.1083)	(22.9831)	(27.2288)	(29.4990)
Pipe 2	7.72225	9.21940	10.78482	11.57265	13.16401	14.74742	15.54325
	(8.71461)	(10.4311)	(12.3148)	(13.3234)	(15.4826)	(17.8424)	(19.1019)
Pipe 3	3.52966	4.98454	6.47281	7.24308	8.80864	10.32311	11.08570
	(2.16675)	(3.50567)	(4.98731)	(5.78491)	(7.50051)	(9.38643)	(10.3971)

Note: We vary the velocity u_1 and we keep other variables fixed. The values in parenthesis refer to the analytical results.

DOI: 10.1002/fld

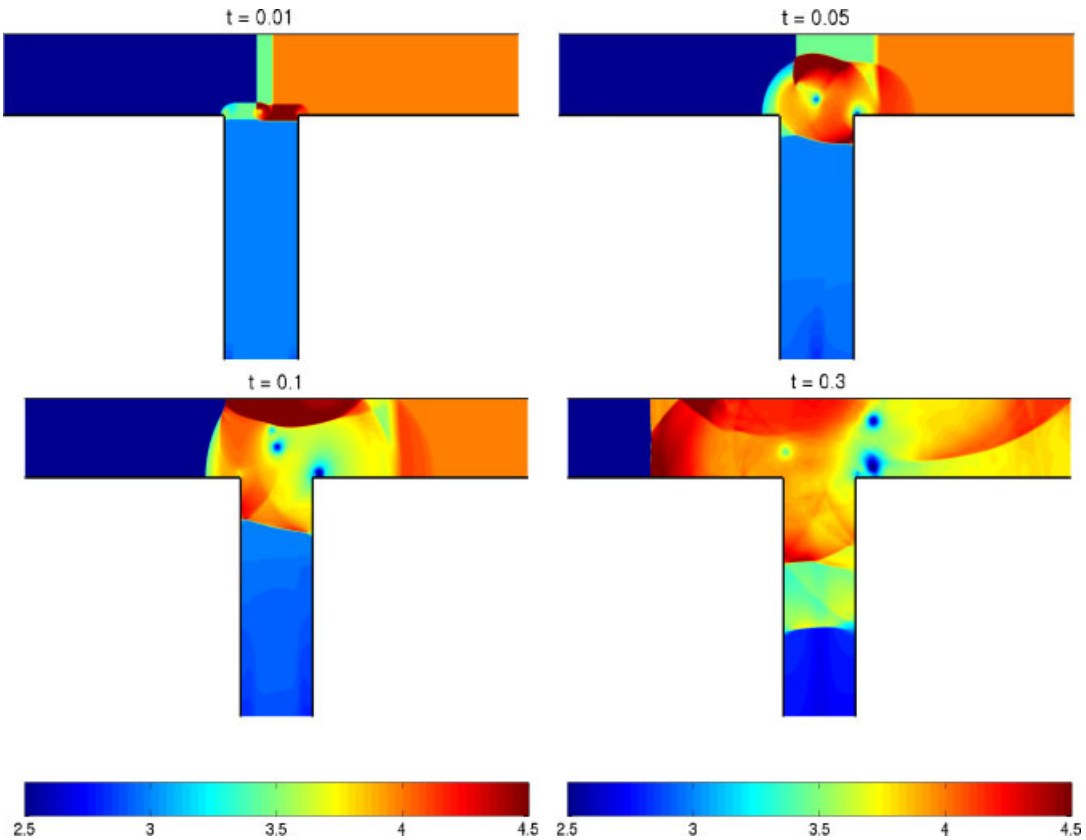

Figure 8. Density snapshots for the 2-to-1 situation at four different times.

situation. Here, we vary the initial density in the first pipe ρ_1 and keep the other initial conditions fixed as in (38). The results of the simulation and the analytical results for the pressure and flux are presented in Tables II and III. The analytical values appearing in Tables II and III are obtained as explained in Section 4.3. For varying density (Table II) the values of the simulation and the analytical results using equal pressure (8) and conservation of mass (7) nearly coincide in the case of the pressure. Furthermore, a nearly constant pressure is observed in the simulation on all three pipes. For the flux value, we observe mass conservation for the simulation results through the pipe fitting in the sense that $\rho_1(u_1 + v_1) = \rho_2(u_2 + v_2) + \rho_3(u_3 + v_3)$. Only for low-density values $\rho_1 \in [2, 2.8]$ the analytical flux values and the simulation values differ significantly. In the case of varying velocity on pipe 1 (Table III) we observe that the simulation results do not match the analytical results. However, the pressure in the simulation results is also nearly constant among the three pipes and the analytical results increases with increasing initial velocity. Again, for the flux values we observe mass conservation in the simulation results and a good coincidence with the analytical results. Furthermore, the trend of the values coincides in the following sense: higher inlet pressure yields also higher outlet pressures on all connected pipes and the increase in the numerical as well as in the theoretical values is of the same order of magnitude. Therefore, we

DOI: 10.1002/fld

Table IV. Verification of coupling conditions for the 2-to-1 situation.

	$\rho_1 = 2$	$\rho_1 = 2.4$	$\rho_1 = 2.8$	$\rho_1 = 3$	$\rho_1 = 3.4$	$\rho_1 = 3.8$	$\rho_1 = 4$
Pressure in the three pipes							
Pipe 1	140.4382	137.3583	156.5741	162.0017	171.4451	178.2517	178.7003
	(148.159)	(157.74)	(166.208)	(170.113)	(177.384)	(184.058)	(87.206)
Pipe 2	132.1602	130.7926	145.0368	149.2337	157.0167	165.3663	172.7972
	(148.159)	(157.74)	(166.208)	(170.113)	(177.384)	(184.058)	(87.206)
Pipe 3	131.9409	135.3705	150.8626	155.6209	163.7195	171.6990	177.0658
	(148.159)	(157.74)	(166.208)	(170.113)	(177.384)	(184.058)	(87.206)
Flux in the three pipes							
Pipe 1	4.66796	6.85069	9.25338	10.62823	13.13057	15.61265	17.03667
	(2.36935)	(5.84284)	(9.08615)	(10.6345)	(13.6047)	(16.4275)	(17.7903)
Pipe 2	7.33813	7.21964	10.04339	11.08653	13.18215	15.19692	16.52907
	(8.62266)	(7.50797)	(6.43258)	(5.90914)	(4.8891)	(3.90234)	(3.42052)
Pipe 3	7.87449	5.77260	7.06037	7.33073	7.88101	8.33301	8.72201
	(10.992)	(13.3508)	(15.5187)	(16.5436)	(18.4938)	(20.3299)	(21.2108)

Note: We vary the density ρ_1 and we keep other variables fixed. The values in parenthesis refer to the analytical results.

have a good qualitatively agreement between the numerical simulation results and the theoretically predicted values. Of course, the fully dynamics as illustrated in Figure 7 demonstrate that it is more complex than one-dimensional model would predict. Summarizing, even though the absolute values of both approaches do not coincide for all settings, we observe similar trends. The equal pressure and mass conservation assumptions for the analysis carried out in [9] are also common to many engineering approaches [20] and are reasonable in this setting.

We now turn our attention to the numerical verification of coupling conditions for the 2-to-1 situation. Again, we consider varying initial data and check for qualitative agreement between numerical and theoretical results. We consider the following initial conditions:

$$\rho_1 = 2, \quad \rho_2 = 4, \quad \rho_3 = 3; \quad u_1 = 5, \quad u_2 = 2.5; \quad v_3 = 4 \tag{39}$$

We use a uniform mesh with $h = 0.01$ and illustrate in Figure 8 the density snapshots at times $t = 0.01, 0.05, 0.1$ and 0.3. Again, low-density regions appear in the shock area located at the junction of the three pipes which have been advected later to pipe 2. It can be clearly seen that the complicated flow structures are being captured by our fifth-order reconstruction. The relaxation scheme perform well for this test situation. We now prescribe density and flux as in Section 3.2 and give the analytical solutions in the equal pressure and conservation of mass case. We present results for varying incoming densities in Table IV.

The most striking difference to the one-dimensional case is the difference in the final pressures in the three pipes. Opposite to the 1-to-2 situation the pressure does not seem to converge to a single pressure value at the intersection. Further, in the volume-averaged flux values we observe differences. They might be due to the fact that the numerical solution is not stationary. Of course,

DOI: 10.1002/fld

the difference in the final pressures also influences the distribution of the fluxes and therefore, the absolute values of the flux in Table IV differ significantly from the theoretical predictions. On the other hand, a similar trend can be observed in both the numerical and theoretical results. Increasing inlet pressure yields an increase of outlet pressures and mass fluxes and therefore, the raise is of the same order of magnitude in both cases. Hence, in this situation the predicted theoretical values obtained by conditions (7) and (8) cannot be supported by numerical results. This might be due to the fact that the geometry of the intersection plays an important role when simulating a combined inflow on two connected arcs. This supports the modelling common in the engineering community where pressure loss factors are introduced near the intersection, see e.g. [21].

6. CONCLUDING REMARKS

We have conducted a numerical study of the most common types of pipe-to-pipe fittings in gas flow by considering a two-dimensional representation of the fitting. Typically, each pipe in a gas network is modelled as a one-dimensional domain to minimize the computational effort. Then, at the tee intersections, coupling conditions have to be imposed. We have compared in this work imposed conditions with simulation results for a two-dimensional situation. The numerical results are carried out by a fifth-order relaxation WENO scheme for the governing equations. The scheme replaces the nonlinear equations of conservation laws by a semilinear hyperbolic system with linear characteristic speeds and easy to solve without relying on Riemann solvers or characteristic decompositions. In addition, the scheme combines a fifth-order WENO reconstruction for the spatial discretization and a TVD Runge–Kutta method for the time integration. The presented results show good shock resolution with high accuracy in smooth regions and without any non-physical oscillations near the shock areas.

The purpose of the two-dimensional numerical simulation of an intersection is to compare qualitatively the predicted effects of common theoretical assumptions with a full numerical simulation. Depending on the considered geometry of the pipe-to-pipe fitting the assertions are partially validated. In both cases the trend of theoretical and numerical results is similar. However, for the 2-to-1 tee fitting, the behaviour predicted by the one-dimensional differs from the results obtained by the simulation. This might be due to the effect of the geometry on the two-dimensional flow pattern. This supports another common modelling approach using geometry and flow-dependent pressure loss factors at the intersection.

Since the main focus of the present work is to establish the ability of simulating coupling conditions at the pipe intersections, the simulation of a full gas network using a two or even three-dimensional model has not yet been carried out and will be subject to future work.

ACKNOWLEDGEMENT

Partial financial support from the German Research Foundation (DFG) Grant DFG Schwerpunktprogramm 1253 is gratefully acknowledged.

REFERENCES

1. Osiadacz AJ. *Simulation and Analysis of Gas Networks*. Gulf Publishing Company: Houston, 1989.
2. Osciadacz AJ. Different transient models—limitations, advantages and disadvantages. *Twenty-eighth Annual Meeting of PSIG* (*Pipeline Simulation Interest Group*), San Francisco, CA, 1996.

DOI: 10.1002/fld

3. Chapmann KS. Virtual pipeline system testbed to optimize the US natural gas transmission pipeline system. *Technology Status Assessment Report*, 2002.
4. Osciadacz AJ. Comparison of isothermal and non-isothermal transient models. *Thirtieth Annual Meeting of PSIG* (*Pipeline Simulation Interest Group*), Denver, CO, 1998.
5. Zhou J, Adewumi MA. Simulation of transient flow in natural gas pipelines. *Twenty-seventh Annual Meeting of PSIG* (*Pipeline Simulation Interest Group*), Albuquerque, NM, 1995.
6. Martin A, Möller M, Moritz S. Mixed integer models for the stationary case of gas network optimization. *Mathematical Programming* 2006; **105**(2–3(B)):563–582.
7. Ehrhardt K, Steinbach M. Nonlinear gas optimization in gas networks. In *Modeling*, *Simulation and Optimization of Complex Processes*, Bock HG, Kostina E, Pu HX, Ranacher R (eds). Springer: Berlin, 2005.
8. Sekirnjak E. Transiente technische optimierung. *Technical Report*, PSI, Berlin, 2000.
9. Banda MK, Herty M, Klar A. Gas flow in pipeline networks. *Networks and Heterogeneous Media* 2006; **1**:41–56.
10. Banda MK, Herty M, Klar A. Coupling conditions for gas networks governed by the isothermal Euler equations. *Networks and Heterogeneous Media* 2006; **1**:295–314.
11. Greyvenstein GP. An implicit method for analysis of transient flows in pipe networks. *International Journal for Numerical Methods in Engineering* 2002; **53**:1127–1143.
12. Wylie EB, Streeter VL. *Fluid Transients in Systems*. Prentice-Hall: Englewood Cliffs, NJ, 1993.
13. Heath MJ, Blunt JC. Dynamic simulation applied to the design and control of a pipeline network. *Journal of the Institute of Gas Engineers* 1969; **9**:261–279.
14. Osiadacz A. Simulation of transient flow in gas networks. *International Journal for Numerical Methods in Fluid Dynamics* 1984; **4**:13–23.
15. Pipeline Simulation Interest Group, www.psig.org
16. Emara-Shabaik HE, Khulief YA, Hussaini I. Simulation of transient flow in pipelines for computer-based operations monitoring. *International Journal for Numerical Methods in Fluids* 2004; **44**:257–275.
17. Zhou J, Adewumi MA. Simulation of transients in natural gas pipelines using hybrid TVD schemes. *International Journal for Numerical Methods in Fluids* 2000; **32**:407–437.
18. Colombo RM, Garavello M. A well-posed Riemann problem for the *p*-system at a junction. *Networks and Heterogeneous Media* 2006; **1**:495–511.
19. Colombo RM, Garavello M. On the *p*-system at a junction. *Control Methods in PDE-Dynamical Systems*, vol. 426. Contemporary Mathematics. AMS: Oxford, 2006.
20. White FM. *Fluid Mechanics*. McGraw-Hill: New York, 2002.
21. Crane Valve Group. Flow of fluids through valves, fittings and pipes. *Crane Technical Paper No. 410*, 1998.
22. Balsara DS, Shu CW. Monotonicity preserving weighted essentially non-oscillatory schemes with increasingly high order of accuracy. *Journal of Computational Physics* 2000; **160**:405–452.
23. Jiang GS, Shu CW. Efficient implementation of weighted ENO schemes. *Journal of Computational Physics* 1996; **126**:202–212.
24. Jin S, Xin Z. The relaxation schemes for systems of conservation laws in arbitrary space dimensions. *Communications on Pure Applied Mathematics* 1995; **48**:235–276.
25. Banda M, Seaïd M. Higher-order relaxation schemes for hyperbolic systems of conservation laws. *Journal of Numerical Mathematics* 2005; **13**:171–196.
26. Seaïd M. Non-oscillatory relaxation methods for the shallow water equations in one and two space dimensions. *International Journal for Numerical Methods in Fluids* 2004; **46**:457–484.
27. Seaïd M. High-resolution relaxation scheme for the two-dimensional Riemann problems in gas dynamics. *Numerical Methods for Partial Differential Equations* 2006; **22**:397–413.
28. Seaïd M, Klar A. Asymptotic-preserving schemes for unsteady flow simulations. *Computers and Fluids* 2006; **35**:872–878.
29. Ehrhardt K, Steinbach M. *Nonlinear Gas Optimization in Gas Networks*: *Modeling*, *Simulation and Optimization of Complex Processes*. Springer: Berlin, 2005.
30. Chen NH. An explicit equation for friction factor in pipe. *Industrial and Engineering Chemistry Fundamentals* 1979; **1**:296–297.
31. Shu CW. Total-variation-diminishing time discretization. *SIAM Journal on Scientific and Statistical Computing* 1988; **9**:1073–1084.
32. Gottlieb S, Shu CW, Tadmor E. Strong stability preserving high order time integration methods. *SIAM Review* 2001; **43**:89–112.
33. Woodward P, Colella P. The numerical simulation of two-dimensional fluid flow with strong shocks. *Journal of Computational Physics* 1984; **54**:115–173.

DOI: 10.1002/fld